A Mask R-CNN Network for Wide-Area Mining Subsidence Automatic Detection With InSAR Observations

Kelu He⦿, Xuesong Zhang⦿, Zhenhong Li⦿, *Senior Member, IEEE*, Wandong Jiang, Jiawei Zhou, and Bingquan Han

Abstract—Land subsidence caused by mining activity is one of the most serious anthropogenic geohazards. The rapid detection and continuous monitoring of mining subsidence facilitate the swift detection of geohazards. The traditional methods of monitoring mining subsidence have shortcomings, such as offering only a limited coverage and being time consuming. Interferometric Synthetic Aperture Radar (InSAR) has been proven to be a powerful tool to identify mining subsidence hazards from unwrapped interferograms, but this method can be complex and inefficient, particularly for wide areas. In this article, a mask R-CNN model is presented to automatically detect mining subsidence and monitor the surface activity over wide areas using original SAR interferograms to avoid the time-consuming and error-prone phase unwrapping procedure. Using Sentinel-1 wrapped interferograms as the real dataset and simulated wrapped interferograms generated with the Gaussian surface function combined with Generic Atmospheric Correction Online Service (GACOS) for InSAR as the simulated dataset, the mask R-CNN deep neural network was used to train the mining subsidence detection model. It turned out that the accuracy of the detection model was 91.48%, while the precision was 96.44%, the recall rate was 93.88%, and the F1 index was 0.949. The detection model was then utilized to detect mining subsidence in southwestern Shanxi, China, between 2016 and 2022. A total of 152 land subsidence points were detected and long-term monitoring results were also obtained. An analysis of the state of land subsidence in the mining areas was carried out to obtain land subsidence activity during the monitoring period.

Kelu He, Xuesong Zhang, Wandong Jiang, Jiawei Zhou, and Bingquan Han are with the College of Geological Engineering and Geomatics, Chang'an University, Xi'an 710054, China, also with the Key Laboratory of Loess, Xi'an 710054, China, and also with the Big Data Center for Geosciences and Satellites, Chang'an University, Xi'an 710054, China (e-mail: hekelu@chd.edu.cn; xuesong.zhang@chd.edu.cn; 2020126041@chd.edu.cn; 2023026005@chd.edu.cn; bingquan.han@chd.edu.cn).

Zhenhong Li is with the College of Geological Engineering and Geomatics, Chang'an University, Xi'an 710054, China, also with the Key Laboratory of Loess, Xi'an 710054, China, and also with the Key Laboratory of Western China's Mineral Resources and Geological Engineering, Ministry of Education, Xi'an 710054, China (e-mail: zhenhong.li@chd.edu.cn).

Index Terms—InSAR, mask R-CNN, mining subsidence, surface activity, time series detection.

I. INTRODUCTION

UNDERGROUND mining often leads to a lowering of the Earth's surface (hereafter referred to as land subsidence) as a result of the collapse of bedrock and the subsequent sinking of unconsolidated surface sediments [1]. Although there is often a time lag between when the underground mining starts and when the mining subsidence occurs, rapid detection and long-term monitoring of land subsidence in mining areas are important elements in the monitoring of mining activity, which is vital for the economic development of mining cities and the safety of people and property. Such monitoring is used to guide underground mining work, facilitate the supervision of mining activities, and allow the timely detection of illegal mining [2].

Currently, mining subsidence can be monitored in a number of ways, from in situ instruments to remote sensing from UAV and satellites. Optical leveling is a traditional method to monitor the mining subsidence. Although offering a high degree of accuracy (at the mm level), spirit leveling is time-consuming, which in turn makes it expensive, particularly when dealing with a wide area (e.g., [3]). The Global Navigation Satellite System (GNSS) is another traditional method to monitor land subsidence, but it, similar to spirit leveling, can only provide point measurements [4]. With the rapid development of unmanned aerial vehicles (UAVs), UAV photogrammetry and Light Detection And Ranging (LiDAR) have been widely used for subsidence monitoring [5], [6]. However, they can only be applied to limited areas (e.g., tens to hundreds of km^2) and struggle to penetrate vegetation.

In the past three decades, Interferometric Synthetic Aperture Radar (InSAR) has gradually become a powerful tool in the monitoring of volcanos [7], earthquakes [8], [9], landslides [10], glaciers [11], [12], and large-scale land deformation [13] and shows unprecedented advantages [14].

Wright and Stow [15] used ERS images to obtain the line of sight (LOS) deformation maps over the Selby coalfield in the U.K. and reported that the interferometric fringes were associated with underground mining activities. Since then, InSAR has been widely used to monitor mining subsidence, which is currently believed to be a powerful and quantitative

tool for this purpose (e.g., [16]). Many scholars have proposed a range of methods to acquire precise mining subsidence, e.g., combining InSAR with mining subsidence prediction models [17], [18], SAR pixel offset tracking technique [19], and combining InSAR with terrestrial 3-D laser scanning [20], [21].

Two categories of approaches have been developed to detect areas with mining subsidence: 1) setting deformation rate thresholds (e.g., [22]) and 2) using machine learning (ML) algorithms (e.g., [23], [24]). For Category I, they mainly work on the mean deformation rate maps derived from InSAR stacking or time-series algorithms, which is easy to be implemented. However, areas with small deformation rates are difficult to detect, even if a region has deformed significantly over a short period of time, the deformation rate will be small if the deformation rate is calculated over a large time span. Another disadvantage of Category I approaches is that phase unwrapping is computationally expensive and slow and additional uncertainties can be introduced. For Category II, several ML-based algorithms have been developed to detect mining subsidence using originally wrapped interferograms. For instance, Schwegmann et al. [25] employed the deep convolutional neural network (CNN) to identify deforming areas, but both the accuracy and recognition ability require further improvement. Rotter and Muron [26] proposed a single-shot multibox detector (SSD) architecture based on visual geometry group (VGG) networks and an algorithm based on Tiny You Only Look Once (TinyYOLOv2) to detect collapsed pits caused by coal mining in wrapped interferograms. Wu et al. [27] managed to automatically detect mining subsidence from wrapped interferograms with the deformation detection network (DDNet) and unwrap the cropped interferogram patches centered on the detected subsidence locations with the phase unwrapping network (PUNet). Previous studies have demonstrated that Category II approaches can be promising to detect mining subsidence, but they failed to determine the subsidence boundaries. In addition, computational efficiency remains a challenge, especially when a large number of SAR images are available.

In this article, a new technical framework is presented to detect mining subsidence and monitor mining activity from a series of originally wrapped interferograms. This framework consists of two key parts: 1) the mask R-CNN model training and 2) the model application. There are three noticeable features of the proposed technical framework. The first noticeable feature is the use of originally wrapped interferograms to detect mining subsidence and map their corresponding boundaries, which is based on the fact that mining subsidence is usually characterized as concentric circles or elliptical fringes in the wrapped interferograms due to the working mode of mining activity. Since ML is particularly good at digesting large amounts of data and identifying patterns or finding anomalies in that data, mask R-CNN, being one of the most powerful object recognition ML algorithms shall be effective for detecting concentric circular or elliptical fringes corresponding to mining subsidence. The second noticeable feature of this technical framework is that the simplest interferogram network is adopted, which is beneficial to the rapid processing

of historical SAR imagery and new acquisitions. The third noticeable feature of this technical framework is that a novel indicator titled surface activity is proposed to indicate how frequently the mining subsidence occurs. The more frequent the occurrence of mining subsidence, the greater the surface active will be.

The mask R-CNN structure is described in Section II. In Section III, the mining subsidence detection technical framework is established. The application of the technical framework to southwestern Shanxi, China is demonstrated in Section IV. Discussions are presented in Section V followed by conclusion in Section VI.

II. ML ALGORITHMS

ML—a popular data analysis method in recent years—automates the learning of sample features by simulating human learning behaviors and continuously reinforcing them [28]. In remote sensing, ML has been widely used in the automatic classification of remote sensing images [29], remote sensing image target monitoring [30], [31], and biomass monitoring [32]. Target detection models, as one of the main and most widespread applications in ML, have undergone many years of development. The current mainstream algorithms include AlexNet [33], GoogleNet [34], visual geometry group network (VGGNet) [35], regions with a convolution neural network (R-CNN) [36], fast R-CNN [37], faster R-CNN [38], SSD [39], and You Only Look Once (YOLOv3) [40].

Mask R-CNN—a pixel-level detection and classification network—is an improved network model based on faster R-CNN. Mask R-CNN fully integrates the features identified by each layer of the CNN network to improve the semantic features and increase the accuracy and resolution of target location detection, thus providing the advantage of pixel-level recognition.

A. Network Model Structure

Based on the faster R-CNN, mask R-CNN utilized a mask branch for the segmentation task to improve the accuracy of target detection. Its target detection algorithm is an R-CNN that not only detects targets but also segments them using deep semantics. This method allows the more accurate localization and vivid representation of target objects. Upon detecting a target, it produces a high-quality segmentation mask that can be used to quickly predict the target [41]. The mask R-CNN model introduces the FPN "top–down" extraction of features at different scales and fuses them with the original convolutional extracted feature map. This solves the problem of being unable to recognize small targets and adding the RPN to the CNN to generate the recommended region, on the basis of which target recognition is completed.

The mask R-CNN model also uses the region of interests (RoI) align method to replace the traditional RoI pooling method, allowing the regression frame to be shifted by a small number of decimal places and thus solving the problem of the misalignment of the faster R-CNN feature map with the original image and reducing the impact on the model accuracy. The RoI align feature maps are not fed into the fully linked

network for classification and regression but are fed into the mask branch, where they are fed through fully convolutional networks (FCNs) [42] to classify the pixels within the proposal one by one. The network structure of the mask R-CNN model used in this article is shown in Fig. 1.

Deep residual network (ResNet) has the advantages of easy optimization and improved accuracy, while its jump connection alleviates the gradient disappearance problem associated with increasing network depth. ResNet50 and ResNet101 are often used as backbone networks for the mask R-CNN model, the only difference being that the ResNet network structure has 6 and 23 blocks of convolution layer (conv4), respectively. ResNet101 is deeper and offers improved target detection accuracy. As such, ResNet101 is chosen herein as the backbone network for feature extraction of the input samples.

Its network structure mainly contains five different convolutional modules (C1–C5), and from C1 to C5, the samples are each downsampled to half of their original sizes. The original samples go through a normal convolutional layer. A step size of 2 pixels is used with C1 for feature extraction of the input samples. These are then fed into C2, which uses a 3×3 pixels maximum pooling layer with a step size of 2 pixels, before it is downsampled and fed into the residual block. The residual block consists of three convolutional layers of 1×1, 3×3, and 1×1 pixels, respectively. The images are passed through the C1–C5 convolutional modules of the ResNet101 network to extract features, respectively, resulting in five feature maps of different sizes. The feature pyramid network (FPN) structure upsamples the upper layer feature map to the same size as the next layer feature map and sums it with the next layer feature map to obtain a new feature map. The new feature map is fed into the RPN and a sliding window is set up to find a suggestion box for the target area of the mining.

B. Model Evaluation Indices

Three metrics are commonly used in deep learning to evaluate the performance of network models: precision (P), recall (R), and accuracy (A), which are calculated as follows:

$$P = \frac{TP}{TP + FP} \tag{1}$$

$$R = \frac{TP}{TP + FN} \tag{2}$$

$$A = \frac{TP + TN}{TP + TN + FP + FN}. \tag{3}$$

True positive (TP) are the positive samples divided into positive samples, true negative (TN) are the negative samples divided into negative samples, false positive (FP) are the negative samples divided into positive samples, and false negative (FN) are the positive samples divided into negative samples. P is the predicted outcome of the sample, R is the original sample, and the two are mutually dependent on and affect each other. $F1$ is a summed average of P and R and can be calculated as follows:

$$F1 = \frac{2TP}{2TP + FN + FP}. \tag{4}$$

The mask R-CNN model typically uses mean pixel accuracy (MPA) and mean intersection over union (MIoU) metrics to evaluate the segmentation results of regression classification. Pixel accuracy (PA) represents the proportion of all pixels correctly predicted by the classification, MPA represents the average percentage of correctly classified pixels for the sample used for accuracy assessment, IoU represents the ratio of intersection over union of the segmentation result to the true mask result, and MIoU represents the average intersection over union result for the sample used for accuracy assessment. MPA and MIoU are calculated as follows:

$$MPA = \frac{1}{n+1} \sum_{s=0}^{n} \frac{P_{ss}}{\sum_{t=0}^{n} P_{st}} \tag{5}$$

$$MIoU = \frac{1}{n+1} \sum_{s=0}^{n} \frac{P_{ss}}{\sum_{t=0}^{n} P_{st} + \sum_{t=0}^{n} P_{ts} - P_{ss}} \tag{6}$$

where P_{ss} denotes the sample category of s predicted to be s, P_{st} denotes the sample category of s predicted to be t, P_{ts} denotes the sample category of t predicted to be s, and n denotes the number of predicted categories. As there is only one category of mining area, n is 1.

III. METHOD DEVELOPMENT

Fig. 2 shows the proposed technical framework for using the mask R-CNN model to identify mining subsidence and monitor its evolution. The mask R-CNN is trained to obtain the mining subsidence detection model, which detects the mining subsidence areas in the wrapped interferograms based on the learned features of mining surface deformation, atmospheric effects, and random noise. When a new wrapped interferogram is available, the mining subsidence detection model can be used to detect the mining areas directly, determine their locations and boundaries, and examine the evolution of the mining areas.

A. Dataset Preparation

The use of ML methods does not require the manual extraction of features but does require a large training dataset. Note that land subsidence in mining areas is affected by a range of conditions, such as mining time, mining depth, and government policy, making it difficult to obtain sufficient real data. This results in a smaller real dataset being collected for model training and validation. In order to solve problems such as low model training accuracy that may be caused by the small number of samples in the real dataset, this article proposes a method by which to simulate InSAR interferograms of land subsidence in mining areas, increasing the number of samples involved in training and validation by producing simulated interferograms. The real and simulated datasets are labeled and used together as the training and validation dataset for the model. The accuracy of the training model is achieved by comparing and analyzing the real dataset, the simulated dataset, and the mixed dataset combining the two, to obtain a mining subsidence detection model based on mask R-CNN.

In this article, Sentinel-1 A/B wrapped interferograms taken from the Yushen and Changzhi mining areas were used
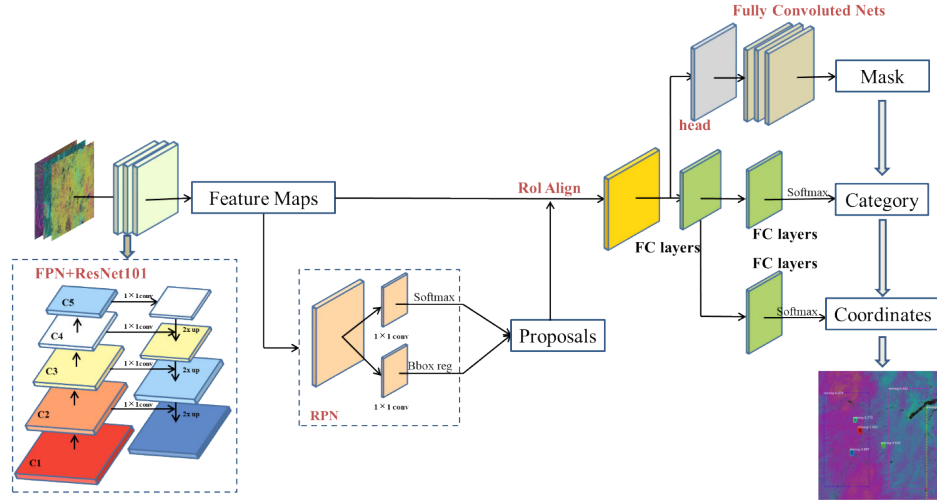
Fig. 1. Network structure of the mask R-CNN model. On the left of the Net, the images are input into the model. At the bottom left of the network, the structure of FPN is illustrated. At the bottom middle, the structure of RPN and activation function used is described. On the right of the Net, the full convolutional network structure and mask branches are shown.

as the real dataset. Sentinel-1A/B SAR images spanning a period of two years were acquired and wrapped interferograms with minimum temporal baselines were generated using the GAMMA software [43], using SRTM DEM and high-accuracy orbital data to remove topographic and orbital phases. The Goldstein filtering method was used to reduce phase noise [44]. The color images used to make the dataset were generated using the default parameters set by the rasmph script (from the GAMMA DISP package). During the production of the dataset, the generated color images were sliced according to an overlap of 34% and a size of 800×800 pixels. Afterward, the land subsidence characteristics of the mining areas were manually labeled on the sliced color interferograms. The result files contained the original images, mask information, and labeled mask images as the standard dataset format for training the network model.

Large-scale, high-intensity underground mining often causes a short-term, rapid surface deformation that exceeds the detection capability of InSAR, which can appear as phase decoherence on InSAR interferograms [45]. At the same time, short wavelength SAR signals, such as X- and C-band, do not penetrate vegetation well, leading to poor imaging quality of InSAR interferograms; this is especially the case in areas with heavy summer vegetation. Therefore, it is difficult to collect a large real dataset of good quality.

In this article, a method for simulating InSAR wrapped interferograms of land subsidence in mining areas is proposed to increase the number and quality of the training dataset; this simulated dataset offers enhanced generalization capability over the real dataset. The InSAR wrapped phase usually contains a deformation phase φ_{def}, atmospheric phase φ_{atm}, and noise phase φ_{noise}, and so, the wrapped phase φ_{wrap} can be expressed by the following equation:

$$\varphi_{\text{wrap}} = \varphi_{\text{def}} + \varphi_{\text{atm}} + \varphi_{\text{noise}}. \tag{7}$$

According to (7), to simulate the InSAR wrapped phase, the deformation phase caused by the land subsidence of the mining area can be modeled using the Gaussian surface function.

By adjusting the parameters, the mining land subsidence area can be obtained for different settlement amounts, boundary ranges, and morphologies. The Gaussian surface function is represented as follows:

$$d_{\text{sim\_def}} = \frac{1}{2\pi\sigma^2} \exp\left(\frac{-\left[(X-u)^2 + (Y-u)^2\right]}{2\sigma^2}\right) \tag{8}$$

where $d_{\text{sim\_def}}$ is the modeled land subsidence, X and Y represent the grid size, u represents the location of the subsidence center, and σ^2 is the variance. The atmospheric phase can generally be divided into those caused by stratified atmosphere and those caused by turbulent atmosphere. The Generic Atmospheric Correction Online Service (GACOS) for InSAR, using the iterative tropospheric decomposition (ITD) model, is applied to separate stratification and turbulence signals from tropospheric delay and to generate high spatial resolution atmospheric delay maps [8]. The simulation of the atmospheric phase in this article was obtained by differencing the atmospheric delay maps obtained by GACOS. The equation for differencing is shown as follows:

$$d_{\text{sim\_atm}} = \text{ZTD}_1 - \text{ZTD}_2 \tag{9}$$

where $d_{\text{sim\_atm}}$ is the simulated atmospheric error, and ZTD_1 and ZTD_2 are the two atmospheric delay maps generated by GACOS at different times. In order to make the simulated atmospheric phase more realistic, multiple pairs of GACOS results were randomly selected for differencing, respectively, among the GACOS results generated in spring, summer, autumn, and winter. Finally, the simulated noise $d_{\text{sim\_noise}}$ was randomly simulated by a continuous uniform distribution.

The process of fusing $d_{\text{sim\_def}}$, $d_{\text{sim\_atm}}$, and $d_{\text{sim\_noise}}$ and wrapping to obtain the simulated wrapped phase can be expressed as

$$\varphi_{\text{sim\_wrap}} = W(d_{\text{sim\_def}} + d_{\text{sim\_atm}} + d_{\text{sim\_noise}}) \tag{10}$$

where $W(\cdot)$ is the wrapping process and $\varphi_{\text{sim\_wrap}}$ is the final obtained simulated phase. The flowchart of the simulated data generation is shown in Fig. 3.
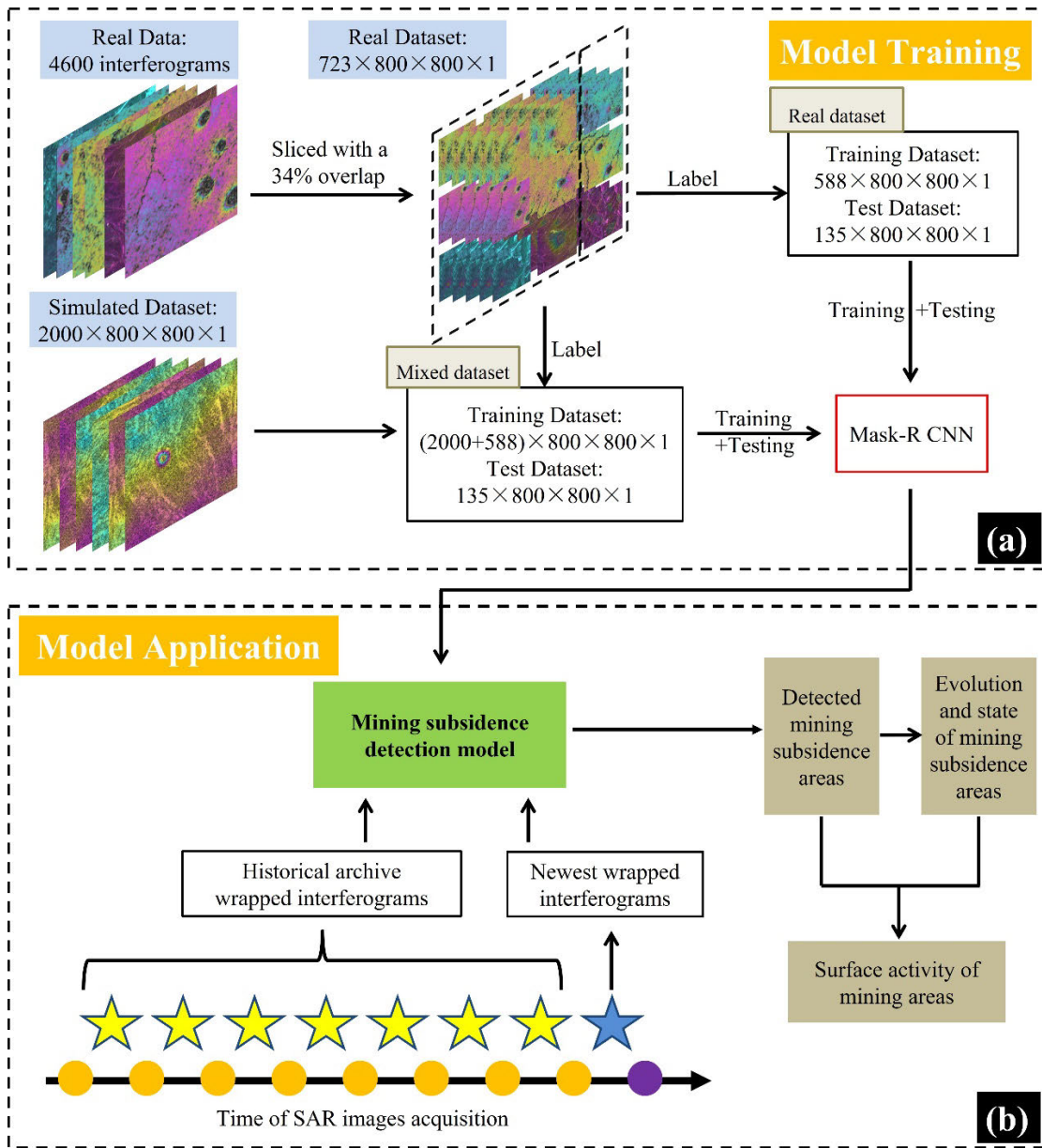
Fig. 2. Technical framework of the mining subsidence detection (a) flowchart of the model training, the interferograms were sliced and labeled to generate the training dataset and test dataset, and then, the mask R-CNN was trained and tested to create the mining subsidence detection model and (b) flowchart of the model application, the orange and purple circles represent the SAR images acquired at different times, while the yellow and blue pentagrams represent the interferograms generated with adjacent SAR images.

B. Long Time Series Mining Subsidence Detection Patterns

In order to examine the evolution of the mining subsidence areas, only the SAR interferograms generated from two adjacent SAR images are employed. To avoid additional uncertainties introduced by phase unwrapping, particularly in areas with large deformation gradients, the wrapped InSAR interferograms are directly utilized to identify the mining subsidence areas. Note that the abovementioned strategies ensure the high efficiency of this proposed technical framework for obvious reasons: 1) the number of the SAR interferograms is minimized with the first strategy and 2) phase unwrapping, the most time-consuming step in interferometric processing, is not required.

As shown in Fig. 2(b), all historical SAR images are co-registered to the same master image, and wrapped interferograms are generated with two adjacent SAR images. Each wrapped interferogram is input into the land subsidence detection model to detect the mining subsidence areas and determine their locations and boundaries. When a newly acquired SAR image is available, the same operation as used for the historical images is then performed to generate a wrapped interferogram together with the most recent SAR image in the historical SAR datasets. Then, the wrapped interferogram can then be input into the model to identify the latest land subsidence areas.

After obtaining the historical and latest land subsidence areas, their evolution can then be determined, and then, the
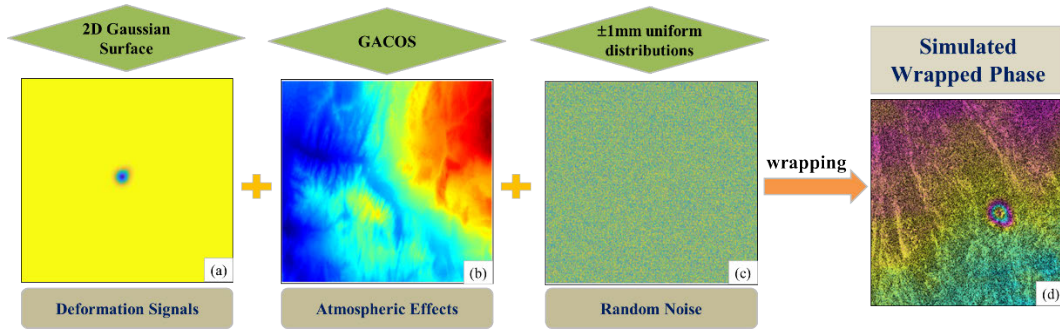
Fig. 3. Simulated InSAR wrapped phase, where (a) is the Gaussian surface function simulating the mining deformation phase, (b) is the GACOS simulated atmospheric phase, (c) is the random noise, and (d) is the simulated mining subsidence wrapped phase.

level of surface activity (i.e., the activity timing and frequency of each land subsidence area) can be assessed. For N scenes of archived historical SAR images, only N − 1 interferograms are generated and no phase unwrapping is needed, which greatly reduces the required storage space and processing time, while avoiding additional uncertainties introduced as a result of unwrapped interferograms. For newly acquired SAR images, there is no need to deal with multiple previous SAR images or to reinvert all interferograms to obtain information, such as the average rate, reducing the huge computational effort and possible mismatch with historical data caused by the addition of new data.

IV. APPLICATION OF SENTINEL-1 DATA TO SOUTHWESTERN SHANXI

Shanxi is located in the North China Plateau, which is the most extensive coal production province in China [46]. Shanxi has exhibited the continuous, ultraintensive, large-scale exploitation of coal resources, which has led to numerous and widespread land subsidence in mining areas [47]. Therefore, southwestern Shanxi was selected as the study area. A total of 132 scenes of Sentinel-1A/B ascending SAR images (see Fig. 4) were collected during the period from October 2016 to March 2022. In order to obtain the surface activity index, only interferograms with the minimum time baselines were generated. The 132 SAR images were acquired at 12-day intervals, resulting in 131 interferograms. All the interferometric processing was conducted using the GAMMA software [43]. All the SAR images were cropped and mosaicked to the appropriate size, before being co-registered to the SAR image acquired on November 26, 2018 (lying central to the collection dates of all the SAR images) and generating interferograms. A 2-pixel multilook operation in the range direction and a 10-pixel multilook operation in the azimuth direction were performed to suppress noise.

The original interferograms were binary grayscale images, which were converted to RGB color images by the rasmph script in GAMMA with default parameters, in order to be better recognized by the deep learning network. The trained mask R-CNN model of the mining areas was applied to these interferograms and periodic land subsidence detection was carried out in the study area, based on which the state of mining-induced land subsidence in the long time series was determined and statistics were produced. Finally, the active

durations of mining-induced land subsidence in the study area were examined in detail.

A. Performance Evaluation of Network Model

The mask R-CNN model used was trained based on the TensorFlow framework. The experiments were set to an epoch of 20, the number of iterations per epoch was 1000, the initial learning rate was 0.0001, and the weight decay factor was 0.005. To avoid local optimal solutions and accelerate the convergence rate, the momentum factor was set to 0.9.

The real dataset comprised 723 real samples, using 80% (588 samples) as the training dataset and 20% (135 samples) as the test dataset. A total of 2588 training samples (including 588 real samples and 2000 simulated samples) were used in the mixed dataset to train the network model. Other parameters in the network model were set identically, and the accuracy of the model was evaluated using the above evaluation indexes. We produced two simulated datasets: one with GACOS and the other one without GACOS, and then trained the model and calculated the detection accuracy. The results are shown in Table I.

It is clear that the use of a simulated dataset increased the number of samples for model training, improved the quality of the samples, and increased the accuracy of the resulting model compared to models trained with real data only. Note that the recall rate decreased (i.e., the detection results of mining subsidence areas corresponded to the number and locations of real markers), indicating that increased accuracy rate has an impact on the recall rate, and the F1 index can better weigh these two evaluation indexes.

As can be seen from Table I, the model trained on the simulated dataset with GACOS generally over performed the model without GACOS, especially in terms of MPA. Analyzing the simulated data without adding the atmospheric errors in the interferograms will weaken the characteristics of the real interferograms, resulting in lower model accuracy. So, the mask R-CNN model, which was trained on a mixed dataset of real data and simulated data with GACOS, was used for the detection of mining subsidence areas and further analysis in subsequent experiments and analyses.

B. Detected Mining Subsidence Areas

Taking seven interferograms containing mining subsidence in the study area as an example, the land subsidence detection
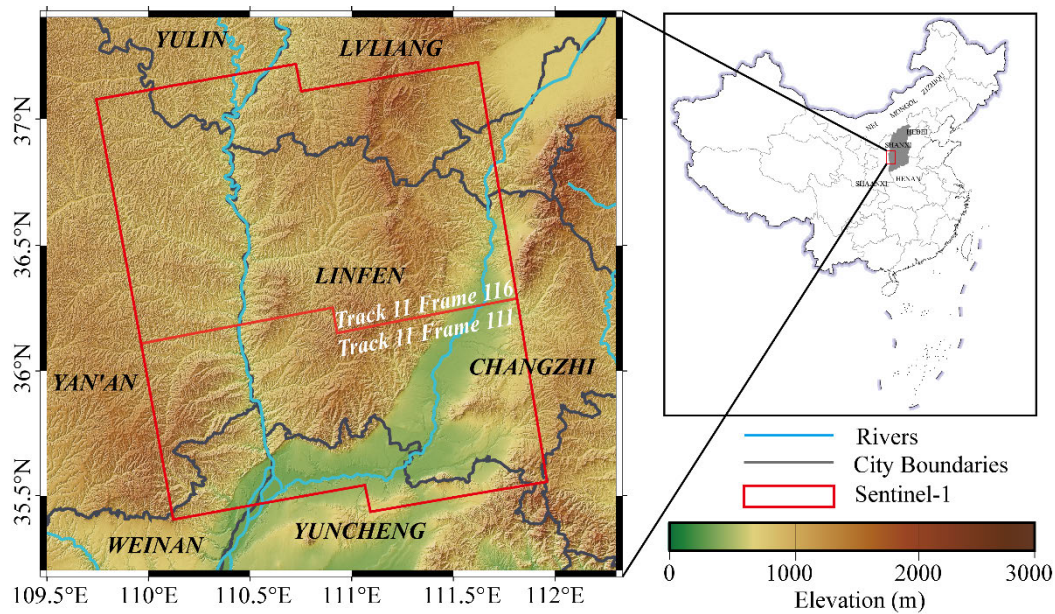
Fig. 4. Study area. The datasets of rivers (blue lines) and city boundaries (gray lines) were obtained on the website of People's Republic of China (PRC) Natural Resources Department. The red borders indicate the coverages of Sentinel-1 A/B images used.

TABLE I
NETWORK MODEL ACCURACY EVALUATION

Dataset	Evaluation indexes					
	P	R	A	MPA	MIoU	F1
Real dataset	95.24%	94.76%	90.94%	63%	53.38%	0.948
Mixed dataset with GACOS	96.44%	93.88%	91.48%	70.82%	57.20%	0.949
Mixed dataset without GACOS	94.05%	93.73%	92.86%	57.78%	52.20%	0.938

model for the mining area was used to detect the images in the experimental area, and the land subsidence locations and boundaries were subsequently obtained (see Fig. 5). In Fig. 5(I)–(VII), (a) shows the interferograms with mining land subsidence features at different locations at different times in the study area and (b) shows the detection results of the mining subsidence detection model corresponding to (a). The detection results include the suggestion boxes and the boundaries of the mining subsidence areas and their corresponding probability.

In Fig. 5, the land subsidence detection model can detect the mining subsidence areas in the interferograms, regardless of the differences in their corresponding RGB colors. The locations and boundaries of the detected mining subsidence areas are consistent with those detected by way of visual recognition. In Fig. 5(I-a), the concentric fringes in the middle part are obvious with nearly rectangular shapes and their corresponding recognition probability is 0.997 [see Fig. 5(I-b)]. The mining subsidence area in the white rectangle of Fig. 5(I-a) is not detected due to the similarity of the color of the interferometric fringes to those of the surrounding area, while the two mining subsidence areas in the white rectangle

of Fig. 5(II-a) are not detected due to the discontinuity of the interferometric fringes caused by low coherence.

Fig. 5(III-a) is of good quality, with good recognition results and offer recognition probabilities exceeding 0.86 and relatively consistent boundaries. The interferogram quality of Fig. 5(IV-a) is also good. From Fig. 5(IV-b), it can be seen that consistency with the visual recognition boundary in Fig. 5(IV-a) is strong, with a recognition probability above 0.95. In Fig. 5(V-a), the interferogram is influenced by the atmosphere during this time period, which is manifested by the obvious differences in color on the original interferogram. However, the overall recognition performance is good and the leakage rate (the proportion of the undetected number to the total number) of this interferogram is 28%. In Fig. 5(V-b), two subsidence areas in the lower left corner are detected as one mining subsidence area due to their close proximity with each other, resulting in the underestimation of the number of mining subsidence areas in the statistics.

The interferogram in Fig. 5(VI-a) is strongly influenced by the atmosphere, but the land subsidence detection model offers a strong detection level, with recognition probability exceeding 0.82 [see Fig. 5(VI-b)]. Although the land
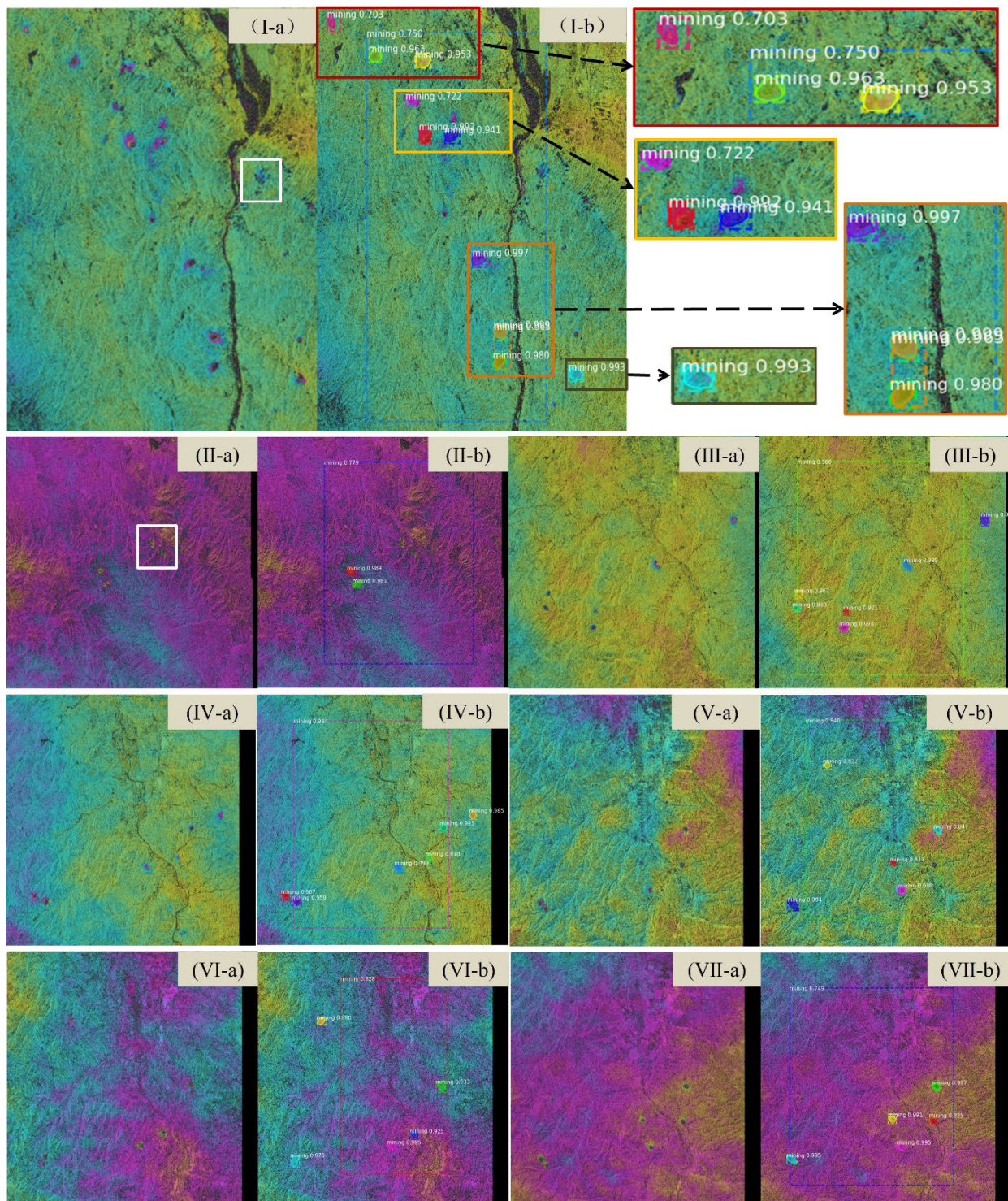
Fig. 5. (a) Original interferograms and (b) results of the mining subsidence detection model. Note that: 1) (I-a)–(VII-a) show the original interferograms with mining land subsidence features at different locations at different times in the study area; 2) (I-b)–(VII-b) show the detection results of the mining subsidence detection model; and 3) Masks are shown in color, and boundary boxes and confidence are also shown.

subsidence in the lower left corner is not visually obvious, it is detected by the model.

Fig. 5(V-a) and (VII-a) is the two independent interferograms acquired in the same area at different times, both of which consist of obvious atmospheric effects and show different RGB color patterns. It can be seen from Fig. 5(V-b) and (VII-b) that their leakage rates are lower than 28% (the calculation method is shown in the above leakage rate), sug-

gesting good performance in both cases in spite of atmospheric effects and hence strong robustness of the mining subsidence detection model.

Combining the sliced detection results provides detection results for the entire study area, and here, the results for the winter, with its reduced vegetation impact, have been selected for presentation, as shown in Fig. 6.
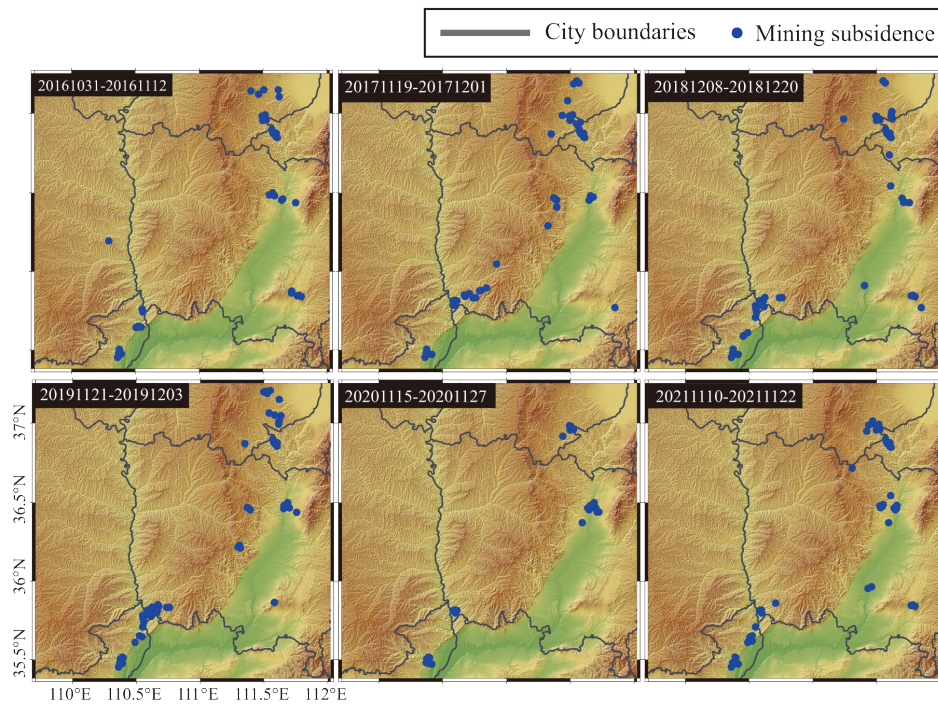
Fig. 6. Mining subsidence detection locations for the study area. Blue dots indicate the detected mining subsidence areas.
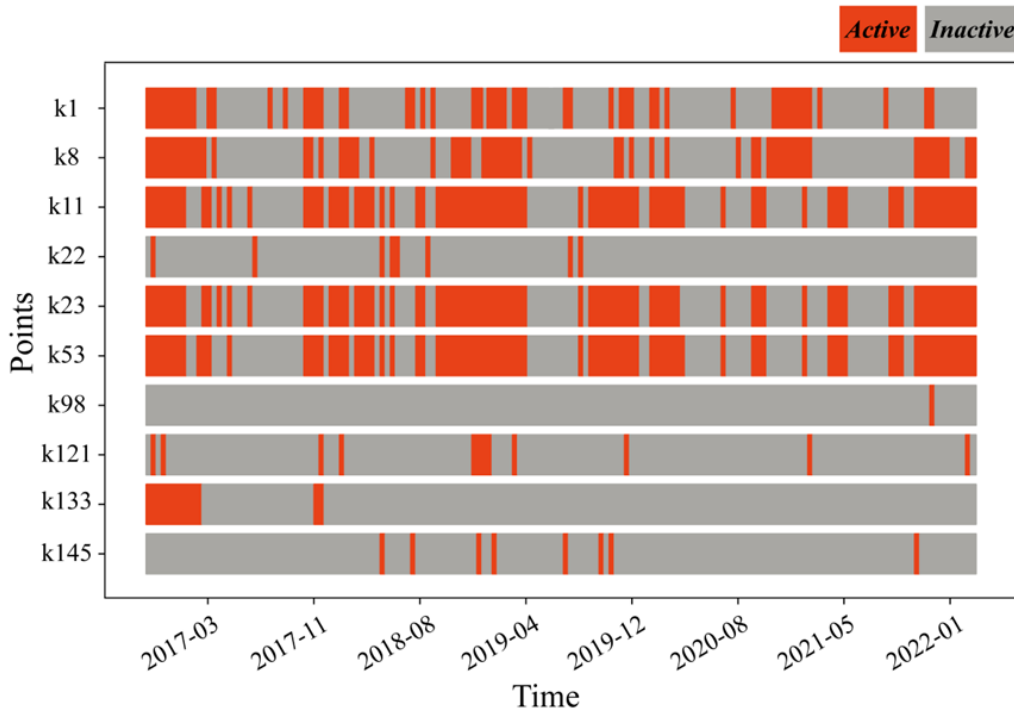
Fig. 7. Long time series of mining subsidence (example of detected locations). Red color indicates where subsidence has been detected and gray color indicates where no obvious subsidence has been detected.

Overall, a total of 152 mining subsidence points (Nos. k1–k152) were detected between 2016 and 2022. During this period, the number of mining subsidence points were relatively uniform, with no sudden increases or decreases, and mining subsidence occurred in the almost same areas, mainly in the northeast and southwest of the study area. It was verified that the land subsidence caused by mining mainly occurred in the Qinshui, Huoxi, and Hedong coalfields, as well as the

Hancheng mining area, and that the distribution of the detected mining subsidence areas was consistent with the distribution of major mines.

C. Evolution of Mining Subsidence

Underground mining in the mining areas leads to an imbalance of stresses in the overlying rock layers, which can cause land subsidence [48]. The extent of land subsidence
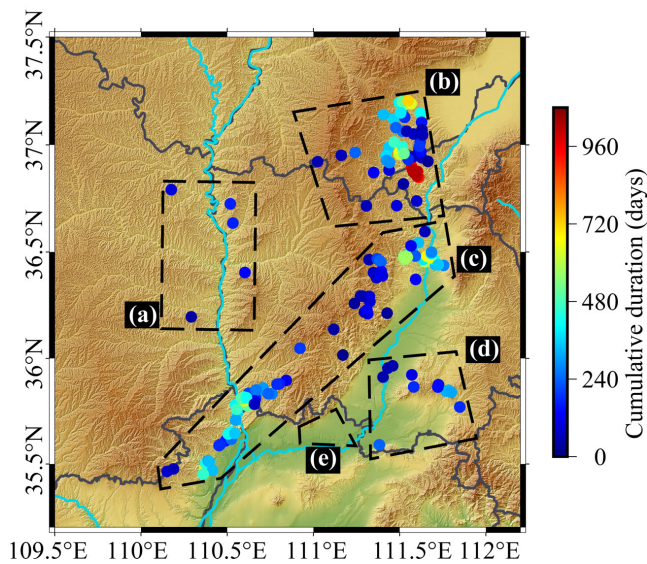
Fig. 8. Map of surface activity (cumulative duration, unit: days). Note that 1) the dot color range from blue to cyan to yellow to red, representing the cumulative duration of ground motion and 2) areas (a)–(e) are selected for further analysis in Fig. 11.
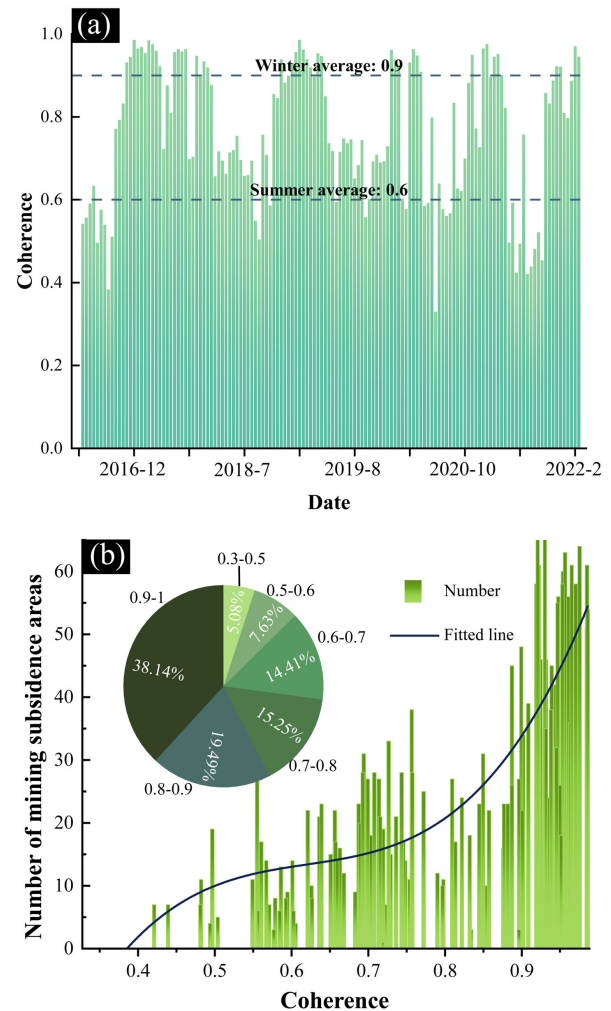

Fig. 9. Coherence statistics (a) is a statistical histogram of the C-band interferometric coherence. The upper blue dashed line represents the average coherence in winter (December, January, and February), while the lower blue dashed line represents the average coherence in summer (June, July, and August) and (b) is the number of detected mining subsidence areas versus the coherence of each interferogram. The blue curve is a fit of the number of detected mining subsidence areas to the coherence, and the pie charts count the percentages of detected mining subsidence areas corresponding to different coherence intervals.

in mining areas is often much larger than the extent of the goaf. Underground mining land subsidence has a certain time lag, with land subsidence usually occurring months to years after mining. It is thus important to monitor land subsidence in mining areas continuously over a long time series.

The long time series (approximately six years) of land subsidence in the study area was obtained by using the model to detect 131 interferograms in Section IV-B, and ten selected subsidence areas are shown in Fig. 7 (see Appendix for full results). In Figs. 13–16, the overall evolution of the detected mining subsidence is more clearly demonstrated. Land subsidence is often not detected during the months of June to August each year, mainly due to the fact that the Sentinel-1A/B (C-band) signals are not able to fully penetrate vegetation during summer. This leads to low coherence and makes it difficult to show concentric circular or elliptical fringes in the interferograms.

In Fig. 7, the mining subsidence is easy to be detected in winter but it is difficult to be detected in summer. Regardless of the influence of summer vegetation on the coherence of the interferogram, it can be divided into the following states: 1) mining subsidence is almost continuous, such as K1, K8, K11, K23, and K53. In addition to the influence of poor quality of the interferogram caused by seasonal factors, these detected points are almost in a continuous subsidence state during the six years; 2) the mining subsidence is discrete, such as K22, K121, and K145. The subsidence of these detected points in the six-year period is discontinuous and discrete, and the subsidence duration is short. These coal seams may be caused by shallow mining, small-scale mining and short time mining; 3) K98 will only detect mining subsidence in a relatively short time at the end of 2021. There may be new mining activity at this time; 4) since 2017, there has been almost no mining subsidence detected at K133. It appears that the mining work

of the corresponding mining face at this point was completed in 2017.

D. Surface Activity

In this article, surface activity is defined as the cumulative duration of ground motion and can provide the basis for a quantitative and qualitative analysis of land subsidence and its influencing factors. It is believed that surface activity can also provide preparatory information for the subsequent prediction and early warning of geological hazards, such as land subsidence [49].

As demonstrated in Fig. 2, the mining subsidence area detection is applied to individual interferograms without time overlapping and the time span of each interferogram is known (i.e., 12 days for most interferograms in this study). Therefore, the surface activity (i.e., cumulative duration) of each pixel can be determined by summing up the time spans of all the
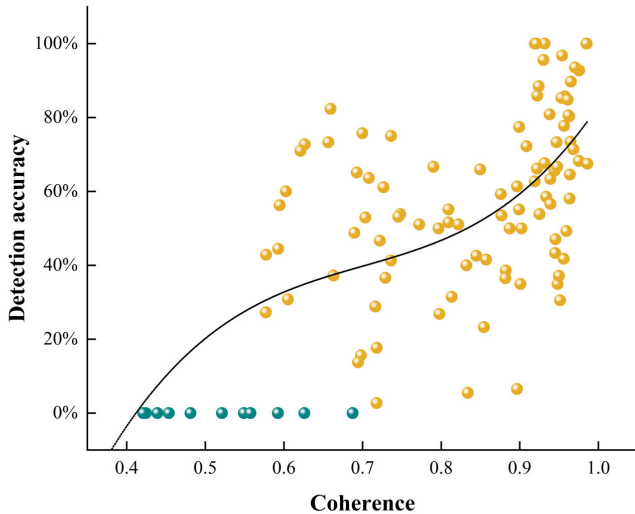
Fig. 10. Relationship between the detection accuracy and coherence. The blue points represent interferograms with a detection accuracy of 0, because no mining area subsidence was visually identified in the interferograms. The yellow points represent the detection accuracy of other interferograms, and the black curve represents the fitting curve between the coherence and detection accuracy.

interferograms, in which the specific pixel is identified as "active." Fig. 8 shows the map of surface activity of the study area during the six-year period. Area (a) is located in Huoxi coalfield, and the cumulative duration of mining subsidence is shorter than 240 days (i.e., 15.3%) from 2016 to 2022, suggesting weak surface activity. Area (b) is located in Qinshui coalfield, and the cumulative durations of mining subsidence mostly range from 240 to 960 days (i.e., 15.3%–61.1%), indicating strong surface activity. Area (c) covers Hancheng coalfield, Huoxi coalfield, and Qinshui coalfield from west to east, and the cumulative durations of mining subsidence vary from 120 to 600 days (i.e., 7.6%–38.2%), implying moderate-to-strong surface activity. Area (d) is located in Qinshui coalfield, and the cumulative duration of mining subsidence is in the range of 120–360 days (i.e., 7.6%–22.9%), suggesting moderate surface activity. No mining subsidence area is detected in area (e).

V. Discussion

A. Interferogram Availability Analysis

One of the main challenges in the detection of using the mining subsidence detection model is whether the subsidence of a mine is clearly characterized in the interferograms. The clarity of features in interferograms is mainly related to coherence. Generally, in midlatitude areas, vegetation is denser in summer than in winter and provides thicker coverage of the ground surface. This means that the coherence of C-band interferograms is generally higher in winter than in summer and the subsidence features are more obvious. As shown in Fig. 9(a), the peak of C-band coherence tends to occur in winter and the trough of coherence tends to occur in summer. The mean value of coherence in winter is 0.9, and in summer, it is 0.6.

Fig. 9(b) shows the relationship between the C-band interferometric coherence and the number of mining subsidence

areas. The pie chart shows the percentages of detected mining subsidence areas corresponding to different coherence intervals, indicating that 57.63% of the mining subsidence areas are detected over pixels with coherence greater than 0.8. The blue curve is fitted to the number of the mining subsidence areas referenced to the coherence. Generally speaking, the number of mining subsidence areas increases with the coherence. It can be seen that only limited mining subsidence areas can be detected when the coherence is less than 0.5. When the coherence is greater than 0.7, the land subsidence detection model performs well.

In order to evaluate the impact of the interferometric coherence on the performance of the detection subsidence model, its detection accuracy was calculated against the average coherence of the wrapped interferogram one by one, and the relationship between the detection accuracy and coherence is shown in Fig. 10. Note that 1) the mining subsidence areas were visually identified using high-resolution satellite images with some of them being verified in the field, and the total number of the identified subsidence areas was considered as the truth number; 2) the detection accuracy is defined as the ratio between the number of the detected subsidence areas from the detection model and the truth number; 3) the detection accuracy is defined as 0 in the case that no mining subsidence area is visually detected areas, which could be due to low coherence or limited mining activity during the specific period; and 4) a total of 110 wrapped interferograms were employed in this evaluation. It is clear in Fig. 10 that 1) when the coherence is less than 0.6, the mining subsidence is difficult to be detected and 2) when the coherence is greater than 0.6, the higher the average coherence is, the higher detection accuracy could be achieved.

It is worth noting that some small deformations can be visually detected that cannot be detected by the detection model, and these points are present in large numbers at certain moments; second, due to certain errors, some interferometric fringes caused by mining subsidence are too blurry and can only be barely detected visually; third, two working faces that are too close apart result in overlapping of interferometric fringes, and these reasons lead to the fact that the relationship between the detection accuracy of the model and the coherence of the interferograms is not linear and in the appearance of some outlier points.

B. Comparison Between Categories I and II Approaches

As mentioned in Section I, Category I approaches often utilize the mean deformation rate maps derived from InSAR stacking or time series algorithms to detect mining subsidence areas. In this study, the multilook and filtering parameters used to generate the interferograms were identical to those mentioned earlier, and a total of 749 interferograms (from 20170312 to 20220310) were obtained by setting the maximum number of connections to six. The SBAS InSAR method [50], [51] was employed to estimate the deformation rate map [see Fig. 11(I)], with the GACOS + PCA method [52] being used to reduce the atmospheric errors. Cluster analysis is one of the techniques that enable to partition
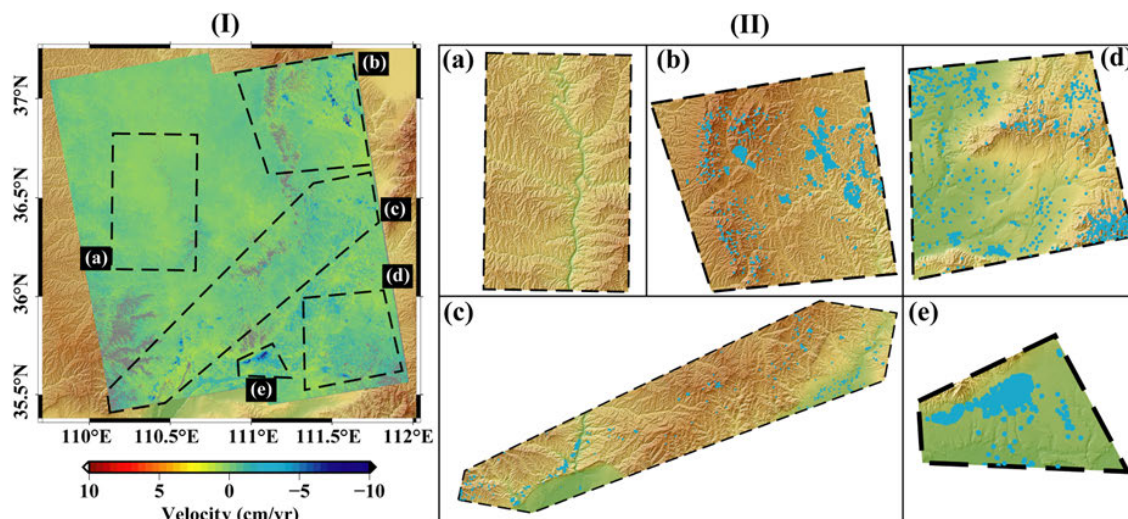
Fig. 11. Deformation rate map and its cluster maps, divided into areas (a)–(e). (I) shows the deformation rate map (cm/yr) and (II) shows the deformation rate clusters of the five selected areas.
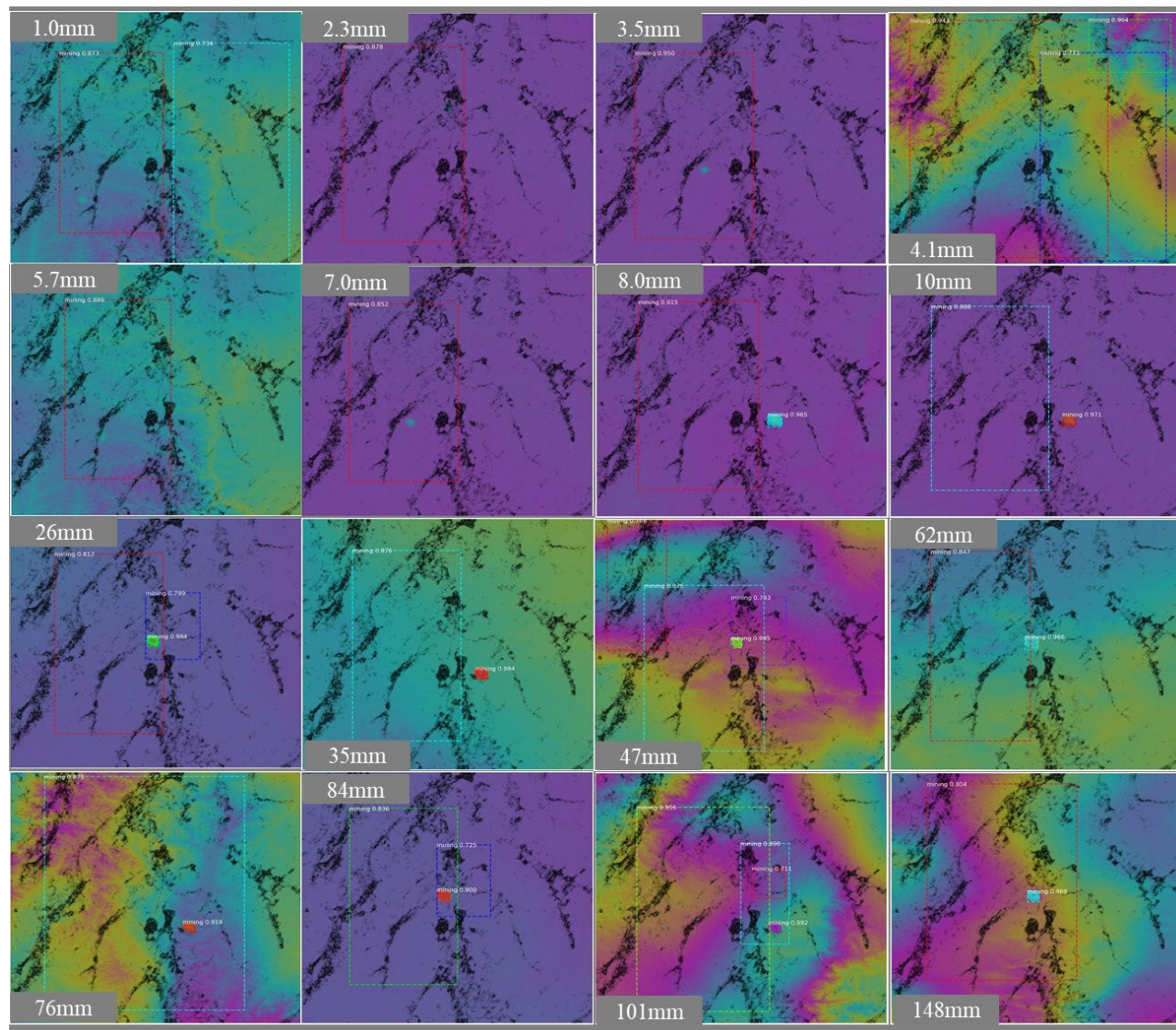

Fig. 12. Simulated interferograms for deformations of varying magnitude from 1 to 148 mm and results from a mining subsidence detection model.

a dataset into subsets (called clusters), so that data points in the same cluster are as similar as possible, and data points in different clusters are as dissimilar as possible. The Getis-Ord G∗i statistic (G∗i), also known as hotspot analysis, is a

Fig. 13. Long time series of mining subsidence in area (a).

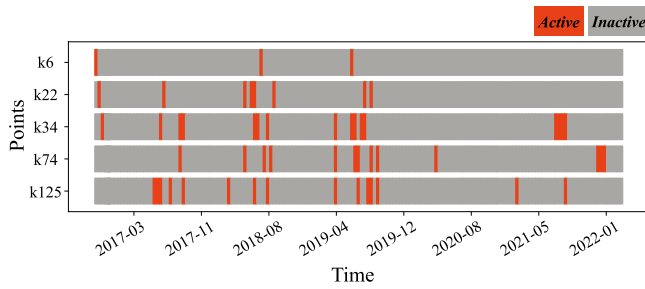Fig. 14. Long time series of mining subsidence in area (b).

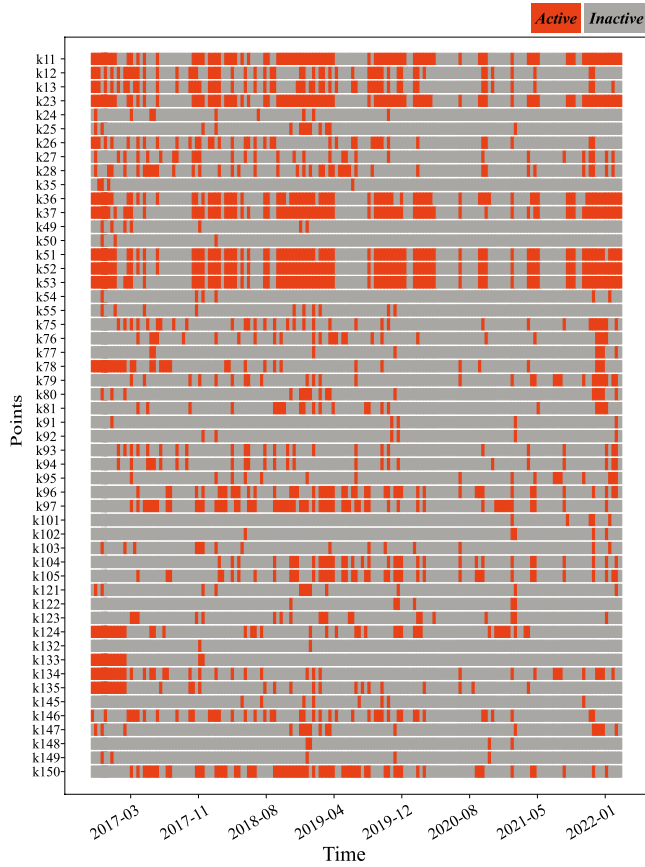Fig. 15. Long time series of mining subsidence in area (c).
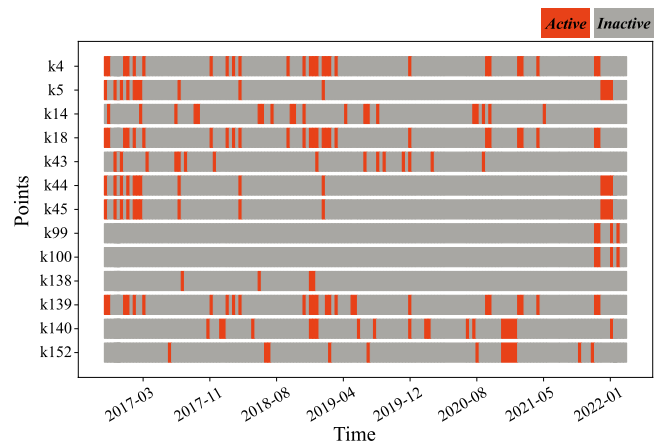
Fig. 16. Long time series of mining subsidence in area (d).

method commonly used to analyze location-related clustering of trends in spatial data attributes, and cluster of deformation rate maps can be used to identify hazard potential points [53]. The deformation rate map was subjected to a hotspot analysis and the results are shown in detail for areas (a–e) in Fig. 11.

In area (a), no mining subsidence area is observed based on the deformation rate map [see Fig. 11(I-a)], while the surface activity map (see Fig. 8) reveals the presence of five mining subsidence areas, suggesting that Category I approaches are less sensitive to areas with low mining activity than the proposed Category II approach in this article.

In area (b), the surface activity map (see Fig. 8) shows strong surface activity with dot color, indicating the cumulative duration of each detected mining subsidence area. Some areas with large cumulative durations are not detected in Fig. 11(I-b), which is most likely due to the loss coherence caused by the large displacement gradients [e.g., the west and south in area (b) of Fig. 8]. On the other hand, it can be seen
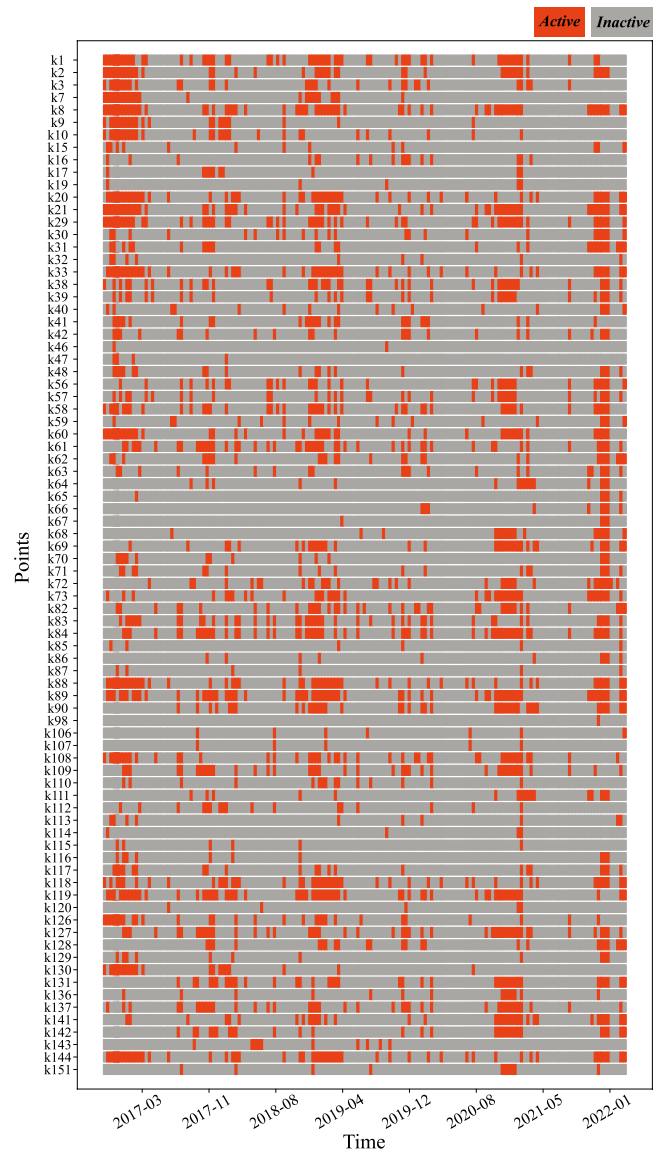
in Fig. 11(II-b) that a large number of deforming areas are detected using the deformation rate map plus cluster analysis approach, but many of those deforming areas are not the result

of mining activity [e.g., the northwest and southwestern area (b) of Fig. 8 accounts for about one quarter].

Part of areas (c) and (d) are located in densely vegetated areas, in which some detected mining subsidence areas in Fig. 8 [e.g., the southeastern area (c) and the southwestern area (d) of Fig. 8] do not appear in those detected through the deformation rate map [see Fig. 11(II-d) and (II-e)]. In the clustering results for area (d) [see Fig. 11(II-d)], some of the mining subsidence areas are incorrectly detected [e.g., the southwestern and southeastern area (d) of Fig. 8].

Fig. 11(I-e) shows the areas with large deformation rates, but no mining subsidence area is detected in the surface activity map (see Fig. 8). A visual interpretation with Google Earth imagery in area (e) shows that there are two large factories in the area, and the subsidence in the area is likely to be caused by groundwater extraction. Since the patterns of the interferometric fringes do not match the characteristics of mining subsidence, the mask R-CNN-based surface activity method is able to remove it from the detected mining subsidence list.

Category I approaches utilize deformation rate maps to identify areas with deformation rates over a given threshold, and they have several limitations to detect mining subsidence areas. First, areas with limited mining activity over short time spans can be easily overlooked in long-term deformation rate maps and are thus assumed to be "inactive," which is problematic and might result in high missing rates. Second, the deformation rate maps are generated from unwrapped interferograms, and phase unwrapping (e.g., [50], [54]) is required for each interferogram. Mining activity often induces surface displacements with large gradients, thus causing coherence loss, which may in turn lead to localized holes (missing values) in the resultant deformation rate maps and then high missing rates in the mining subsidence area detection. Third, large storage and high computation time are required to generate deformation rate maps. For InSAR time series algorithms, a new inversion shall be performed when a new SAR acquisition is available, which can be time-consuming and make it difficult for rapid detection of mining subsidence over wide regions.

In contrast, the proposed Category II approach (i.e., the mask R-CNN-based surface activity method) can not only be used to detect mining subsidence areas from individual wrapped interferograms but also examine the evolution of each detected mining subsidence area. The surface activity method is sensitive to areas with limited mining activity, even those only lasting for short periods. Since only interferograms with the minimum time baselines (i.e., those with adjacent SAR acquisitions) are employed and neither phase unwrapping nor time series inversion are needed, the requirements of data storage and computation time are low.

C. What Is the Minimum Detectable Surface Displacement?

Interferograms with different mining subsidence signals were simulated by Gaussian surface function to assess the minimum detectable surface displacements. A total of 90 interferograms were simulated with 1–148-mm subsidence and then detected using the mining subsidence detection model.

It can be seen in Fig. 12 that when the mining subsidence is ≥8 mm, it can be easily detected with the displacement boundaries being clearly determined; when the mining subsidence is <8 mm, the mining subsidence detection model can only detect the rough area without the displacement boundaries, which is likely due to the following two reasons: 1) the amount of mining subsidence signals is limited that there is no clear subsidence feature in these interferograms and 2) the interferograms are disturbed by atmospheric effects and random noises, and such small displacement signals do not show the subsidence features. Therefore, it is believed that the theoretically minimum detectable deformation simulated using Gaussian surface function in wrapped interferograms of the mining subsidence detection model is approximately 8 mm. It should be noted that since the wrapped interferograms are used to detect mining subsidence in the proposed detection model, the displacement gradient might be another key factor affecting the detection performance.

VI. CONCLUSION

In this article, the mask R-CNN-based surface activity method is presented to detect mining subsidence areas from individual wrapped interferograms and then to examine their evolutions. The mask R-CNN model is used as the base model for detection, and originally, wrapped interferograms generated from two adjacent SAR images are used as the dataset for detection. The following are the main conclusions of this study.

1) A method combining the Gaussian function and GACOS for generating simulated datasets in mining areas is proposed, and it is evident that the simulated dataset benefits to train the detection model.
2) A mask R-CNN model-based detection model for mining subsidence is constructed, which can effectively detect the mining surface subsidence areas from wrapped interferograms, saving the computation time and reducing additional uncertainties introduced by phase unwrapping and time series inversions.
3) A total of 152 surface subsidence areas are detected in the study area during the period from 2016 to 2022 using the surface subsidence detection method, and their evolutions are carefully examined.

It is believed that the mask R-CNN-based surface activity method is an efficient approach to detect mining activity and then monitor the evolutions of the mining subsidence areas, including their locations and boundaries. However, it should be noted that this method is not designed to monitor the magnitudes of the resultant surface displacements, which could refer to [54].

APPENDIX

The long time series (approximately six years) of mining subsidence in the study area was obtained using the land subsidence detection model to detect 131 interferograms, as shown in Section IV-B. Figs. 13–16 show the time series of mining subsidence for areas (a)–(d), respectively. Note that there is no detected area in area (e).

REFERENCES

[1] Z. Qin et al., "Study of ground movement in a mining area with geological faults using FDM analysis and a stacking InSAR method," *Frontiers Environ. Sci.*, vol. 9, Dec. 2021, Art. no. 787053.

[2] Z. Hu, L. L. Ge, X. J. Li, and C. Rizos, "Designing an illegal mining detection system based on DinSAR," in *Proc. 30th IEEE Int. Geosci. Remote Sens. Symp. (IGARSS)*, Honolulu, HI, USA, Jul. 2010, pp. 3952–3955.

[3] D. Dzurisin, "Results of repeated leveling surveys at Newberry Volcano, Oregon, and near Lassen Peak Volcano, California," *Bull. Volcanol.*, vol. 61, nos. 1–2, pp. 83–91, Jul. 1999.

[4] S. Choy, S. Bisnath, and C. Rizos, "Uncovering common misconceptions in GNSS precise point positioning and its future prospect," *GPS Solutions*, vol. 21, no. 1, pp. 13–22, Jan. 2017.

[5] Q. Meng et al., "Time-series analysis of the evolution of large-scale loess landslides using InSAR and UAV photogrammetry techniques: A case study in Hongheyan, Gansu Province, Northwest China," *Landslides*, vol. 18, no. 1, pp. 251–265, Jan. 2021.

[6] R. Luo, Z. Zhou, X. Chu, W. Ma, and J. Meng, "3D deformation monitoring method for temporary structures based on multi-thread LiDAR point cloud," *Measurement*, vol. 200, Aug. 2022, Art. no. 111545.

[7] K. Spaans and A. Hooper, "InSAR processing for volcano monitoring and other near-real time applications," *J. Geophys. Res. Solid Earth*, vol. 121, no. 4, pp. 2947–2960, 2016.

[8] C. Yu, Z. Li, and N. T. Penna, "Triggered afterslip on the southern Hikurangi subduction interface following the 2016 kaikōura earthquake from InSAR time series with atmospheric corrections," *Remote Sens. Environ.*, vol. 251, Dec. 2020, Art. no. 112097.

[9] K. Dai et al., "Interpretation and sensitivity analysis of the InSAR line of sight displacements in landslide measurements," *GIScience Remote Sens.*, vol. 59, no. 1, pp. 1226–1242, Aug. 2022.

[10] Y. Shen et al., "Rapid and automatic detection of new potential landslide based on phase-gradient DInSAR," *IEEE Geosci. Remote Sens. Lett.*, vol. 19, pp. 1–5, 2022.

[11] L. Gray, "Using multiple RADARSAT InSAR pairs to estimate a full three-dimensional solution for glacial ice movement," *Geophys. Res. Lett.*, vol. 38, no. 5, Mar. 2011, Art. no. L05502. [Online]. Available: https://agupubs.onlinelibrary.wiley.com/action/showCitFormats?doi=10.1029%2F2010GL046484

[12] L. Liu, L. Jiang, H. Jiang, H. Wang, N. Ma, and H. Xu, "Accelerated glacier mass loss (2011–2016) over the puruogangri ice field in the inner Tibetan Plateau revealed by bistatic InSAR measurements," *Remote Sens. Environ.*, vol. 231, Sep. 2011, Art. no. 111241.

[13] M. Peng et al., "Mapping land subsidence and aquifer system properties of the willcox basin, arizona, from InSAR observations and independent component analysis," *Remote Sens. Environ.*, vol. 271, Mar. 2022, Art. no. 112894.

[14] Z. Li, W. Zhu, C. Yu, Q. Zhang, and Y. Yang, "Development status and trends of Imaging Geodesy," *Acta Geodaetica et Cartographica Sinica*, vol. 52, no. 1, pp. 1805–1834, 2023.

[15] P. Wright and R. Stow, "Detecting mining subsidence from space," *Int. J. Remote Sens.*, vol. 20, no. 6, pp. 1183–1188, Jan. 1999.

[16] A. H.-M. Ng et al., "Deformation mapping in three dimensions for underground mining using InSAR—Southern highland coalfield in New South Wales, Australia," *Int. J. Remote Sens.*, vol. 32, no. 22, pp. 7227–7256, Nov. 2011.

[17] L. Zhang et al., "Long-term ground multi-level deformation fusion and analysis based on a combination of deformation prior fusion model and OTD-InSAR for longwall mining activity," *Measurement*, vol. 161, Sep. 2020, Art. no. 107911.

[18] X. Ding et al., "Time series monitoring and prediction of coal mining subsidence based on multitemporal InSAR technology and GSM-HW model," *J. Appl. Remote Sens.*, vol. 16, no. 3, Sep. 2022, Art. no. 038505.

[19] Z. Yang et al., "An alternative method for estimating 3-D large displacements of mining areas from a single SAR amplitude pair using offset tracking," *IEEE Trans. Geosci. Remote Sens.*, vol. 56, no. 7, pp. 3645–3656, Jul. 2018.

[20] B. Chen, K. Deng, H. Fan, and M. Hao, "Large-scale deformation monitoring in mining area by D-InSAR and 3D laser scanning technology integration," *Int. J. Mining Sci. Technol.*, vol. 23, no. 4, pp. 555–561, Jul. 2013.

[21] C. Zhang, Y. Zhao, X. He, J. Guo, and Y. Yan, "Space-sky-surface integrated monitoring system for overburden migration regularity in shallow-buried high-intensity mining," *Bull. Eng. Geol. Environ.*, vol. 80, no. 2, pp. 1403–1417, Feb. 2021.

[22] M. Przyłucka, G. Herrera, M. Graniczny, D. Colombo, and M. Béjar-Pizarro, "Combination of conventional and advanced DInSAR to monitor very fast mining subsidence with TerraSAR-X data: Bytom city (Poland)," *Remote Sens.*, vol. 7, no. 5, pp. 5300–5328, Apr. 2015.

[23] B. Chen et al., "Time-varying surface deformation retrieval and prediction in closed mines through integration of SBAS InSAR measurements and LSTM algorithm," *Remote Sens.*, vol. 14, no. 3, p. 788, Feb. 2022.

[24] N. Anantrasirichai et al., "Deep learning framework for detecting ground deformation in the built environment using satellite InSAR data," 2020, *arXiv:2005.03221*.

[25] C. P. Schwegmann, W. Kleynhans, J. Engelbrecht, L. W. Mdakane, and R. G. V. Meyer, "Subsidence feature discrimination using deep convolutional neural networks in synthetic aperture radar imagery," in *Proc. IEEE Int. Geosci. Remote Sens. Symp. (IGARSS)*, Jun. 2017, pp. 4626–4629.

[26] P. Rotter and W. Muron, "Automatic detection of subsidence troughs in SAR interferograms based on convolutional neural networks," *IEEE Geosci. Remote Sens. Lett.*, vol. 18, no. 1, pp. 82–86, Jan. 2021.

[27] Z. Wu, T. Wang, Y. Wang, R. Wang, and D. Ge, "Deep learning for the detection and phase unwrapping of mining-induced deformation in large-scale interferograms," *IEEE Trans. Geosci. Remote Sens.*, vol. 60, 2022, Art. no. 5216318.

[28] D. Silver et al., "Mastering the game of Go with deep neural networks and tree search," *Nature*, vol. 529, no. 7587, pp. 484–489, Jan. 2016.

[29] Y. Chen, Z. Lin, X. Zhao, G. Wang, and Y. Gu, "Deep learning-based classification of hyperspectral data," *IEEE J. Sel. Topics Appl. Earth Observ. Remote Sens.*, vol. 7, no. 6, pp. 2094–2107, Jun. 2014.

[30] Y.-L. Chang, A. Anagaw, L. Chang, Y. Wang, C.-Y. Hsiao, and W.-H. Lee, "Ship detection based on YOLOv2 for SAR imagery," *Remote Sens.*, vol. 11, no. 7, p. 786, Apr. 2019.

[31] Y. Wang, C. Wang, H. Zhang, Y. Dong, and S. Wei, "A SAR dataset of ship detection for deep learning under complex backgrounds," *Remote Sens.*, vol. 11, no. 7, p. 765, Mar. 2019.

[32] L. Han et al., "Modeling maize above-ground biomass based on machine learning approaches using UAV remote-sensing data," *Plant Methods*, vol. 15, no. 1, pp. 1–19, Dec. 2019.

[33] A. Krizhevsky, I. Sutskever, and G. E. Hinton, "ImageNet classification with deep convolutional neural networks," *Commun. ACM*, vol. 60, no. 6, pp. 84–90, May 2017.

[34] P. Tang, H. Wang, and S. Kwong, "G-MS2F: GoogLeNet based multi-stage feature fusion of deep CNN for scene recognition," *Neurocomputing*, vol. 225, pp. 188–197, Feb. 2017.

[35] K. Simonyan and A. Zisserman, "Very deep convolutional networks for large-scale image recognition," 2014, *arXiv:1409.1556*.

[36] R. Girshick, J. Donahue, T. Darrell, and J. Malik, "Rich feature hierarchies for accurate object detection and semantic segmentation," in *Proc. 27th IEEE Conf. Comput. Vis. Pattern Recognit. (CVPR)*, Columbus, OH, USA, Jun. 2014, pp. 580–587.

[37] R. Girshick, "Fast R-CNN," in *Proc. IEEE Int. Conf. Comput. Vis. (ICCV)*, Dec. 2015, pp. 1440–1448.

[38] S. Q. Ren, K. M. He, R. Girshick, and J. Sun, "Faster R-CNN: Towards real-time object detection with region proposal networks," in *Proc. 9th Annual Conf. Neural Inf. Process. Syst. (NIPS)*, Montreal, QC, Canada, 2015, pp. 1–9.

[39] W. Liu et al., "SSD: Single shot MultiBox detector," in *Proc. 14th Eur. Conf. Comput. Vis. (ECCV)*, Amsterdam, The Netherlands, 2016, pp. 21–37.

[40] J. Redmon and A. Farhadi, "YOLOv3: An incremental improvement," 2018, *arXiv:1804.02767*.

[41] M. Chen, F. Bai, and Z. Gerile, "Special object detection based on mask RCNN," in *Proc. 17th Int. Conf. Comput. Intell. Secur. (CIS)*, Nov. 2021, pp. 128–132.

[42] E. Shelhamer, J. Long, and T. Darrell, "Fully convolutional networks for semantic segmentation," *IEEE Trans. Pattern Anal. Mach. Intell.*, vol. 39, no. 4, pp. 640–651, Apr. 2017.

[43] U. Wegmüller and C. Werner, "Gamma SAR processor and interferometry software," in *Proc. 3rd ERS Symp. Space at Service Our Environ.*, Florence, Italy, 1997, pp. 1687–1692.

[44] R. M. Goldstein and C. L. Werner, "Radar interferogram filtering for geophysical applications," *Geophys. Res. Lett.*, vol. 25, no. 21, pp. 4035–4038, Nov. 1998.

[45] Z. Li et al., "Interferometric synthetic aperture radar for deformation mapping: Opportunities, challenges and the outlook," *Acta Geod. Cartogr. Sin.*, vol. 51, no. 7, pp. 1485–1519, 2022.

[46] L. Haibin and L. Zhenling, "Recycling utilization patterns of coal mining waste in China," *Resour., Conservation Recycling*, vol. 54, no. 12, pp. 1331–1340, Oct. 2010.

[47] Z. Yi et al., "Long-term Landsat monitoring of mining subsidence based on spatiotemporal variations in soil moisture: A case study of Shanxi province, China," *Int. J. Appl. Earth Observ. Geoinf.*, vol. 102, Oct. 2021, Art. no. 102447.

[48] Y. Cheng and Z. Pan, "Reservoir properties of Chinese tectonic coal: A review," *Fuel*, vol. 260, Jan. 2020, Art. no. 116350.

[49] G. Li et al., "Surface deformation evolution in the Pearl River Delta between 2006 and 2011 derived from the ALOS1/PALSAR images," *Earth, Planets Space*, vol. 72, no. 1, pp. 1–14, Dec. 2020.

[50] P. Berardino, G. Fornaro, R. Lanari, and E. Sansosti, "A new algorithm for surface deformation monitoring based on small baseline differential SAR interferograms," *IEEE Trans. Geosci. Remote Sens.*, vol. 40, no. 11, pp. 2375–2383, Nov. 2002.

[51] C. Zhang et al., "An integrated framework for wide-area active landslide detection with InSAR observations and SAR pixel offsets," *Landslides*, vol. 19, no. 12, pp. 2905–2923, Dec. 2022.

[52] X. Zhang, Z. Li, and Z. Liu, "Reduction of atmospheric effects on InSAR observations through incorporation of GACOS and PCA into small baseline subset InSAR," *IEEE Trans. Geosci. Remote Sens.*, vol. 61, pp. 1–15, 2023, doi: 10.1109/TGRS.2023.3281783.

[53] B. Chen et al., "Wide area detection and distribution characteristics of landslides along Sichuan expressways," *Remote Sens.*, vol. 14, no. 14, p. 3431, Jul. 2022.

[54] D. T. Sandwell and E. J. Price, "Phase gradient approach to stacking interferograms," *J. Geophys. Res., Solid Earth*, vol. 103, no. 12, pp. 30183–30204, Dec. 1998.

Zhenhong Li (Senior Member, IEEE) received the B.Eng. degree in geodesy from the Wuhan Technical University of Surveying and Mapping (now Wuhan University), Wuhan, China, in 1997, and the Ph.D. degree in GPS, geodesy, and navigation from University College London, London, U.K., in 2005.

He is currently a Professor of imaging geodesy with the College of Geological Engineering and Geomatics, Chang'an University, Xi'an, China, the Vice Director of the Key Laboratory of Loess, Xi'an, and the Director of the Key Laboratory of Western China's Mineral Resource and Geological Engineering, Ministry of Education, Xi'an. He is also the Principal Investigator of the Generic Atmospheric Correction Online Service (GACOS) for interferometric synthetic aperture radar. His research interests include imaging geodesy and its applications to geohazards (e.g., earthquakes, landslides, and land subsidence) and precision agriculture.

Dr. Li is a fellow of the International Association of Geodesy and an Associate Editor of *Advances in Space Research and Remote Sensing*.

Wandong Jiang received the B.S. and M.Sc. degrees from the Chang'an University, Xi'an, China. He is currently pursuing the Ph.D. degree with the National University of Defense Technology, Changsha, China.

He is also a member of the Big Data Center for Geosciences and Satellites (BDCGS), Xi'an. His research interests include machine learning and landslides.

Jiawei Zhou received the B.E. degree from the Xi'an University of Science and Technology, Xi'an, China, in 2021. She is currently pursuing the Ph.D. degree with the College of Geological Engineering and Geomatics, Chang'an University, Xi'an.

She is also a member of the Big Data Center for Geosciences and Satellites (BDCGS), Xi'an. Her research interests include InSAR and mining subsidence.

Kelu He received the M.Sc. degree from the Xi'an University of Science and Technology, Xi'an, China, in 2021. She is currently pursuing the Ph.D. degree with the College of Geological Engineering and Geomatics, Chang'an University, Xi'an.

She is also a member of the Big Data Center for Geosciences and Satellites (BDCGS), Xi'an. Her research interests include InSAR and machine learning.

Xuesong Zhang received the B.S. degree from the Chang'an University, Xi'an, China, in 2019, where he is currently pursuing the Ph.D. degree with the College of Geological Engineering and Geomatics.

He is also a member of the Big Data Center for Geosciences and Satellites (BDCGS), Xi'an. His research interests include advance SAR and InSAR techniques.

Bingquan Han received the M.Sc. degree in Chang'an University, Xi'an, China, in 2020, where he is currently pursuing the Ph.D. degree.

He is also a member of the Big Data Center for Geosciences and Satellites (BDCGS), Xi'an. His research interests include InSAR and earthquake cycle.